# Simulations of the Solid, Liquid, and Melting of 1-*n*-Butyl-4-amino-1,2,4-triazolium Bromide

**Saman Alavi**

*Steacie Institute for Molecular Sciences, National Research Council of Canada, Ottawa, Ontario K1A 0R6, Canada*

**Donald L. Thompson\***

*Department of Chemistry, University of Missouri−Columbia, Columbia, Missouri 65211*

Molecular dynamics simulations are used to study the solid and liquid properties and to predict the melting point of 1-*n*-propyl-4-amino-1,2,4-triazolium bromide ([patr][Br]) using a force field based on the one developed by Canongia Lopes et al. (*J. Phys. Chem. B* **2004,** *108,* 2038) for dialkyl substituted imidazolium salts, which was modified by including terms from the general AMBER force field. Electrostatic charges for the intermolecular interactions were determined from gas-phase ab initio electron structure calculations of the triazolium cation. Simulations of the solid state at 100 K reproduced the experimental density to within 4%. Simulations from 100 K to the melting point and the liquid from 333 to 500 K were performed to determine the temperature dependence of the densities of the two phases. The structures of the solid and liquid phases are characterized with radial distribution functions, which show that there are strong spatial correlations among neighboring ion pairs in liquid [patr][Br]. The dynamic behavior of the ions in the liquid state is also studied by computing velocity autocorrelation functions and the mean-square displacements between the ions. The melting point is determined by simulating void-induced melting. Changes in the density, intermolecular energy, and Lindemann index are used as indicators of the melting transition. The computed melting point is 360 ± 10 K, which is within 10% of the experimental value 333 K.

## 1. Introduction

Room-temperature ionic liquids (RTILs) are currently receiving a lot of attention as candidates to replace volatile organic solvents because they are more environmentally benign. Also, they are attractive candidates for use in many applications because of the wide range of properties that can be achieved by variations in the structures of the ions.[1,2] We have been exploring the use of molecular dynamic simulations to predict the properties of ionic materials. Here, we report the results of a study of the physical properties of the solid and liquid phases and the melting of 1-*n*-propyl-4-amino-1,2,4-triazolium bromide ([patr][Br]) (see Figures 1 and 2 for molecular and crystal structures, respectively). One of the goals of this study is to determine whether generally available force fields can be used to accurately predict the melting point of a complex ionic solid. Another purpose of the work is to further explore the applicability of void-induced melting simulations for predicting the melting points of complex materials.

We have been investigating a practical method for simulating melting in which the phase transition is induced by introducing voids in the solid simulation supercell. This method is free of some of the difficulties of other theoretical methods for predicting melting points and thus can provide a practical means of determining melting points and an atomic-level understanding of the mechanistic details of melting. One of our goals is to demonstrate that this approach, originally applied to atomic solids,[3−5] is applicable to materials of any complexity. We have used the method of void-induced melting to calculate the melting points of molecular solids (argon[6] and nitromethane[7]) and complex ionic solids (ammonium dintramide,[8] ammonium nitrate,[9] and 1-ethyl-3-methylimidazolium hexafluourophosphate[10]). The method appears to be robust and applicable to
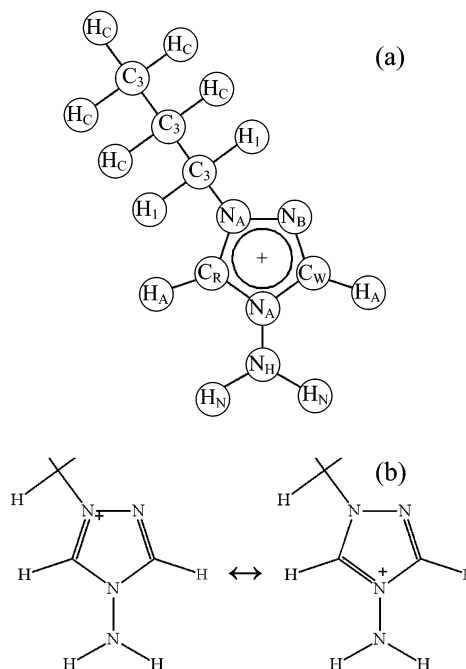


**Figure 1.** (a) Atomic labels of the [patr][Br] ion pair corresponding to the AMBER/OPLS scheme. (b) The two resonance structures of [patr]$^+$. The $N_A$ atoms have positive charge in the resonance structures.

materials with fairly complex structures. Our initial results indicate that a fixed-charge force field that accurately reproduces the solid-state properties of a material can be used to predict the melting point to within about 10% of experiment; however, further study is needed to ascertain the reliability of these kinds of force fields.
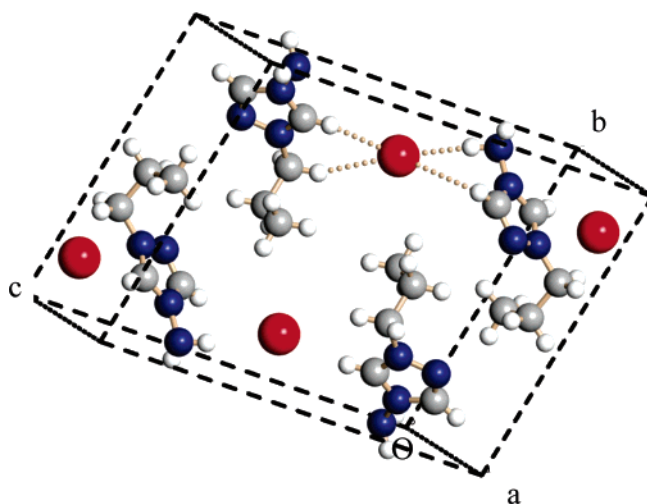
**Figure 2.** Unit cell of [patr][Br] from crystallographic data given by Drake et al.[21] The red spheres represent bromide ions, the blue spheres nitrogen, the gray spheres carbon, and the white spheres hydrogen atoms. Figure courtesy of G. Drake.

The melting of a perfect crystal occurs by a homogeneous nucleation mechanism,[11] which involves a free energy barrier to the formation of the solid−liquid interface that results in superheating of the solid. Thus, heating a perfect crystal with periodic boundary conditions in a molecular dynamics (MD) simulation leads to an overestimation of the equilibrium melting point. Introducing vacancies or void defects in the simulation supercell effectively reduces the free energy barrier to the formation of a solid−liquid interface; thus, as the number of vacancies in the solid is increased, the calculated melting point drops, leveling off at a "plateau temperature" which is taken as the melting point.[3−10] In practice, we observe that the melting plateau is reached when between 6 and 10% of the molecules or ion pairs in the simulation cell are removed. If more than about 10% voids are introduced in the simulation cell, the solid is mechanically unstable and collapses.

Sorescu et al.[12] recently reviewed the details of the void-induced melting method, the direct solid−liquid NVE simulation method of Morris and Song,[13] and the thermodynamic integration method[14] used to determine melting points. Some new method developments that have subsequently appeared are mentioned below.

The thermodynamic integration method for determining the melting point is based on the equality of the free energy of the solid and liquid phases at the melting point. Usually, the free energies of the solid and liquid phases are determined by thermodynamic integration at points away from the melting temperature. Extrapolation is used to find the temperature at which the two free energies are equal. Originally, the absolute values of the free energies of the solid and liquid phases were determined by calculating a thermodynamic pathway connecting the solid and liquid phases to ideal systems for which analytical expressions for the free energy are known. For example, the real liquid is connected to the ideal gas state and the real solid is connected to the ideal Einstein solid. In practice, this method has difficulties, as the thermodynamic integration of the solid state often encounters singularities.

Grochola[15] has recently developed an alternative thermodynamic pathway which directly links the solid state to the liquid, via a "pseudosupercritical transformation". Eike, Brennecke, and Maginn[16] have modified some of the details of this method and used it to determine the melting point of the Lennard-Jones and NaCl solids. The crucial step in this method involves the liquid-

to-solid transformation via a hypothetical three-step process. In the first step, the intermolecular interactions in the liquid phase are gradually turned off and the molecules in the liquid are allowed to rearrange. In the second step, the volume of the simulation cell is decreased and Gaussian potential wells are turned on at locations corresponding to the lattice sites of the solid phase. The molecules are expected to relax into these Gaussian wells. In the third step, the intermolecular interactions are returned to their initial strength. The free energy changes for all three steps of this process can be calculated, thus allowing the determination of three free energy differences between the solid and liquid phases at a given pressure and temperature.

In principle, this method is thermodynamically rigorous, but its application to complex ionic materials such as [patr][Br] with long, flexible side chains has not yet been carried out to our knowledge. The second step of the procedure presents a challenge in applications to complex ions or molecules, as different types of Gaussian wells will be required to fix all of the different and flexible components of a complex structure in the proper lattice locations.

Recently, Luo et al.[17] suggested using the superheating/supercooling temperatures in perfect crystal and liquid simulations to determine the equilibrium melting point. They have used their method to predict the melting point of the Lennard-Jones solid. The method is said to be general[17] and to provide an independent pathway for determining the melting point, but to our knowledge, it has not been applied to complex materials. The superheating and supercooling temperatures required in this method to calculate the equilibrium melting temperature may be difficult to calculate for complex molecular and ionic materials. This is indeed the case for [patr][Br] where the superheating temperature could not be determined by incremental heating (see below).

An important requirement for the simulation of the solid-to-liquid transition is an accurate force field. Many of the standard force fields were developed with the parametrization based on matching of the properties of solids or liquids but not the transition between the phases. Thus, it is important that the reliability of various force fields for describing melting be determined. The testing of force fields for RTILs is less extensive than for organic solids, and thus, one of our interests is to determine the accuracy of existing force fields and ways they can be modified when necessary to achieve acceptable accuracy in predicting melting points.

The force field used in the present study is based on the potential of Canongia Lopes et al.[18] developed for 1-alkyl-3-methyl-imidazolium salts. It is based on the AMBER[19] OPLS[20] all-atom force field. Canongia Lopes et al. validated their force field by comparing simulation results to experimental data for 14 imidazolium salts. We use this potential as a basis for the simulation of [patr][Br] but have modified it by adding some parameters specific to the triazole ring taken from the general AMBER force field (GAFF).[19] None of the force field parameters were adjusted to improve the agreement of the calculated physical properties of [patr][Br] with experimental values. We wish to determine the accuracy for the predictions of melting points with force fields parametrized with data for only the solid and liquids.

## 2. Force Field

The chemical structure of [patr][Br], including labeling of the atoms that we use, is shown in Figure 1a. The triazole ring in [patr]$^+$ has two resonance structures where the positive charge resides on the nitrogen atoms labeled $N_A$. The solid-state structure was determined by X-ray crystallography at 100 K by Drake et al.[21] The unit cell of [patr][Br] is shown in Figure 2.

**TABLE 1: Intramolecular Potential Parameters for [patr][Br]**

| bonds | $k_r$ (kJ/mol·Å²) | $r_{eq}$ (Å) |
|---|---|---|
| $N_H-H_N{}^a$ | 1816.3 | 1.010 |
| $N_A-N_H{}^a$ | 1915.0 | 1.400 |
| $N_A-C_R{}^b$ | 1996.0 | 1.315 |
| $N_{A/B}-C_W{}^b$ | 1787.0 | 1.378 |
| $C_{R/W}-H_A{}^a$ | 1533.4 | 1.08 |
| $N_A-N_B{}^a$ | 2259.4 | 1.347 |
| $N_A-C_3{}^b$ | 1410.0 | 1.466 |
| $H_{1/C}-C_3{}^a$ | 1430.5 | 1.09 |
| $C_3-C_3{}^b$ | 1121.0 | 1.529 |

| harmonic angles | $k_\theta$ (kJ/mol·rad²) | $\theta_{eq}$ (deg) |
|---|---|---|
| $H_N-N_H-H_N{}^a$ | 170.3 | 110.16 |
| $H_N-N_H-N_A{}^a$ | 210.4 | 107.89 |
| $N_H-N_A-C_{R/W}{}^a$ | 277.4 | 118.59 |
| $C_R-N_A-C_W{}^b$ | 292.6 | 108.00 |
| $N_A-C_R-H_A{}^b$ | 146.3 | 125.10 |
| $N_A-C_R-N_A{}^b$ | 292.6 | 109.80 |
| $N_{A/B}-C_W-H_A{}^b$ | 146.3 | 122.00 |
| $N_A-C_W-N_B{}^b$ | 292.6 | 109.80 |
| $C_R-N_A-N_B{}^a$ | 290.0 | 114.37 |
| $C_R-N_A-C_3{}^b$ | 292.6 | 126.40 |
| $N_B-N_A-C_3{}^a$ | 277.4 | 118.84 |
| $C_W-N_B-N_A{}^a$ | 308.4 | 104.16 |
| $N_A-C_3-H_1{}^b$ | 313.2 | 110.70 |
| $N_A-C_3-C_3{}^b$ | 418.4 | 112.70 |
| $H_1-C_3-H_1{}^b$ | 276.1 | 107.80 |
| $H_1-C_3-C_3{}^b$ | 313.2 | 110.70 |
| $C_3-C_3-C_3{}^b$ | 418.4 | 112.70 |
| $C_3-C_3-H_C{}^b$ | 313.2 | 110.70 |
| $H_C-C_3-H_C{}^b$ | 276.1 | 107.80 |

| dihedral angles | $V_1$ | $V_2$ | $V_3$ |
|---|---|---|---|
| $*-N_A-N_H-H_N$ | 0.00 | 10.04 | 0.00 |
| $*-N_A-C_R-*{}^b$ | 0.00 | 19.46 | 0.00 |
| $*-C_W-N_B-*{}^a$ | 0.00 | 40.17 | 0.00 |
| $*-C_W-N_A-*{}^b$ | 0.00 | 12.55 | 0.00 |
| $*-N_A-N_B-*{}^a$ | 0.00 | 40.17 | 0.00 |
| $C_R-N_A-C_3-H_1{}^b$ | 0.00 | 0.00 | 0.00 |
| $C_W-N_A-C_3-H_1{}^b$ | 0.00 | 0.00 | 0.55 |
| $C_W-N_A-C_3-C_3{}^b$ | −5.76 | 4.43 | 0.00 |
| $C_R-N_A-C_3-C_3{}^b$ | −3.23 | 0.00 | 0.877 |
| $N_A-C_3-C_3-C_3{}^b$ | 0.738 | −0.681 | 1.02 |
| $N_A-C_3-C_3-H*{}^b$ | 0.00 | 0.00 | 0.00 |
| $C_3-C_3-C_3-H*{}^b$ | 0.00 | 0.00 | 1.531 |
| $H*-C_3-C_3-H*{}^b$ | 0.00 | 0.00 | 1.331 |
| $*-N_A-*-*{}^b$ | 0.00 | 8.37 | 0.00 |
| $*-C_{R/W}-*-*{}^b$ | 0.00 | 9.2 | 0.00 |

[a] From the GAFF.[19]  [b] Values of the parameters are from Canongia Lopes et al.[18]

The simulations were performed with a fully flexible, all-atom force field based on the one developed by Canongia Lopes et al.[18] for dialkylimidazolium salts. The triazolium cation has atom types not present in the imidazolium salts of ref 18; thus, additional parameters are required to describe [patr][Br], which we have taken from the GAFF given in the AMBER 7 program.[19] In particular, the atom types $N_B$, $N_H$, $H_A$, and Br are specific to [patr][Br] and thus force field parameters relevant to these atoms are taken from GAFF. The intramolecular part of the force field of [patr][Br] has the functional form

$$V(\text{intra}) = \sum_{\text{bonds}} k_r(r - r_{eq})^2 + \sum_{\text{angles}} k_\theta(\theta - \theta_{eq})^2 +$$

$$\sum_{\text{dihedrals}} \sum_{i=1}^{3} \frac{V_i}{2}[1 + (-1)^{i-1}\cos(i\phi)] \quad (1)$$

Harmonic functions with the force constants $k_r$ and $k_\theta$ describe

the intramolecular bond stretching and angle bending motions, respectively, and a cosine series describes the torsional motions. The sums are taken over all bonds, angles, and dihedrals in [patr]⁺. The values of the force constants and other parameters of eq 1 are given in Table 1, where the labeling of the atoms in the [patr][Br] molecule corresponds to Figure 1a.

The intermolecular force field consists of a pairwise additive atom–atom 12-6 Lennard-Jones (LJ) potential for the van der Waals interactions and electrostatic (ES) interactions between point charges centered on the atoms:

$$V(\text{inter}) = \sum_{i=1}^{N-1}\sum_{j>i}^{N}\{V^{\text{LJ}}(r_{ij}) + V^{\text{ES}}(r_{ij})\} \quad (2)$$

with

$$V^{\text{LJ}}(r_{ij}) = 4\epsilon_{ij}^0\left[\left(\frac{\sigma_{ij}^0}{r_{ij}}\right)^{12} - \left(\frac{\sigma_{ij}^0}{r_{ij}}\right)^{6}\right] \quad (3)$$

and

$$V^{\text{ES}}(r_{ij}) = f_{ij}\frac{q_i q_j}{4\pi\epsilon_0 r_{ij}} \quad (4)$$

where the $\epsilon_{ij}^0$ values are the energy minima for the LJ interactions for atoms $i$ and $j$ on different ions and the $\sigma_{ij}^0$ values are the interatomic separations at the potential zero. The values of the LJ parameters for like-atom interactions are given in Table 2 and are taken from the force field of Canongia Lopes et al.[18] and AMBER 7.[19] The values of the parameters for the energies and distances between different atom types are obtained from the standard combination rules, that is, $\epsilon_{ij}^0 = \sqrt{\epsilon_{ii}^0\epsilon_{jj}^0}$ and $\sigma_{ij}^0 = \sqrt{\sigma_{ii}^0\sigma_{jj}^0}$.

The electrostatic atom-centered charges of atoms $i$ and $j$ are $q_i$ and $q_j$, and $\epsilon_0$ is the dielectric permittivity constant for a vacuum. According to the convention of the OPLS potential, electrostatic forces for intramolecular 1,4-interactions have $f_{ij} = 0.5$, since forces between these atoms also contribute through 1,4-dihedral interactions. All other intramolecular interactions separated by more than three bonds are assigned $f_{ij} = 1$. Electrostatic charges are estimated by natural population analysis[22] from an ab initio calculation on a gas-phase [patr]-[Br] molecule at the MP2/6-311G(d,p) level of theory. The calculations were performed with the Gaussian 98 suite of programs.[23] The electrostatic atom-centered charges used in the simulations are given in Table 2. In the two resonance structures

**TABLE 2: Atomic Charges and Lennard-Jones Interaction Parameters of [patr][Br][a]**

| atom[a] | $q$ (e)[b] | $\sigma$ (Å) | $\epsilon$ (kJ/mol) |
|---|---|---|---|
| $N_H$ | −0.474 56 | 3.25 | 0.711 28 |
| $N_A{}^c$ | −0.175 32; −0.098 02 | 3.25 | 0.711 28 |
| $N_B$ | −0.217 01 | 3.25 | 0.711 28 |
| $C_R{}^c$ | 0.307 03 | 3.55 | 0.298 28 |
| $C_W{}^c$ | 0.212 89 | 3.55 | 0.292 88 |
| $C_3{}^c$ | −0.128 55; −0.316 37; −0.507 91 | 3.50 | 0.276 14 |
| $H_N$ | 0.331 61; 0.295 40 | | 0.0000 |
| $H_A{}^c$ | 0.249 76; 0.177 44 | 2.42 | 0.125 52 |
| $H_1{}^c$ | 0.229 78; 0.185 67 | 2.50 | 0.125 52 |
| $H_C{}^c$ | 0.165 60; 0.183 57; 0.156 44 0.179 30; 0.192 18 | 2.50 | 0.125 52 |
| $Br{}^c$ | −0.948 96 | 3.77 | 0.664 07 |

[a] The designation of the atoms is shown in Figure 1a. [b] Charges are from ab initio calculations (see text). [c] Values of the Lennard-Jones parameters are from Canongia Lopes et al.[18]

**TABLE 3: Experimental and Calculated Unit Cell Parameters and Density for Solid [patr][Br] at 100 K[a]**

|  | *a* | *b* | *c* | *ρ* |
|---|---|---|---|---|
| experiment[b] | 5.1237 | 10.9430 | 15.681 | 1.653 |
| calculated | 5.0568 | 10.7998 | 15.476 | 1.717 |

*[a]* The values of *a*, *b*, and *c* are in angstroms, and *ρ* is in grams per cubic centimeter. *[b]* From Drake et al.[21]

of the triazolium ring shown in Figure 1b, the $N_A$ atoms have a formal positive charge, and they also carry more positive charge than the $N_B$ atom in the force field as well. The results of Table 2 show that the positive charge in the ring is predominantly localized at the site of the $C_R$ and $C_W$ atoms.

## 3. Simulation Method

Constant pressure and temperature (NPT) molecular dynamics simulations for $6 \times 3 \times 2$ supercells with 144 [patr][Br] ion pairs have been performed with the DL_POLY program, version 2.10,[24] with the Nosé–Hoover thermostat/barostat algorithm[25,26] and the Melchionna et al.[27] modification. The relaxation times used for the thermostat and barostat are 0.1 and 2.0 ps, respectively. The equations of motion are integrated using the Verlet leapfrog scheme.[28] All interatomic interactions between the atoms in the simulation box and the nearest image sites were calculated within a cutoff distance of $R_{cutoff} = 12$ Å. The Coulombic long-range interactions were calculated using Ewald's method, with a precision of $1 \times 10^{-6}$.[28,29] Constant volume and energy (NVE) simulations were performed to determine the dynamical properties of liquid [patr][Br]. The initial configurations and velocities for the NVE simulations were taken from equilibrated liquid NPT simulations.

We performed MD calculations in the temperature and pressure ranges from 100 to 600 K and from 1.013 25 bar (1 atm) to 7.5 GPa. The initial configuration for the melting simulations was the experimental crystal structure at 100 K, the unit cell of which is shown in Figure 2. The time step for the simulations was 2.0 fs; the system was equilibrated for a minimum of 100 fs (50 000 time steps), and averages were computed over the remaining time of the 700 ps (350 000 time steps) simulation. For temperatures where the melting transition occurred during the simulation, the run times were extended for 100 000 time steps to obtain converged averages of the liquid-state properties.

To avoid superheating in melting simulations, voids were randomly introduced in the simulation supercell. Each void corresponds to the removal of a [patr][Br] ion pair from the supercell and is equivalent to introducing a Schottky defect.[4,30] The simulations of the supercells with voids were performed with conditions identical to those for the perfect crystal.

## 4. Results and Discussion

**A. Solid- and Liquid-State Properties.** At 100 K, solid [patr]-[Br] crystallizes in the triclinic $P\bar{1}$ space group with four molecules per unit cell ($Z = 4$) and unit cell parameters $a = 5.1237$ Å, $b = 10.9430$ Å, $c = 15.681$ Å, $\alpha = 105.777°$, $\beta = 92.264°$, and $\gamma = 99.091°$.[21] An initial set of calculations were performed to obtain values of the solid- and liquid-state properties of [patr][Br]. The crystallographic and calculated unit cell parameters and densities for solid [patr][Br] at 100 K from a NPT simulation with isotropic expansion are given in Table 3. The calculated density of the solid at 100 K of $1.717 \pm 0.002$ g/cm³ is within 4% of the experimental value.

The variations of the densities of the solid and liquid with temperature in the range from 100 to 500 K are given in Table 4 and plotted in Figure 3. The liquid-state density at the

**TABLE 4: Temperature Variation of the Density, *ρ*, for Solid and Liquid [patr][Br] at Ambient Pressure**

| temperature (K) | *ρ* (g/cm³) | temperature (K) | *ρ* (g/cm³) |
|---|---|---|---|
| 100 | $1.717 \pm 0.002$ | 350 | $1.458 \pm 0.008$ |
| 150 | $1.686 \pm 0.003$ | 375 | $1.446 \pm 0.008$ |
| 200 | $1.669 \pm 0.004$ | 400 | $1.430 \pm 0.008$ |
| 250 | $1.641 \pm 0.005$ | 425 | $1.419 \pm 0.008$ |
| 300 | $1.606 \pm 0.005$ | 450 | $1.407 \pm 0.008$ |
| 325 | $1.596 \pm 0.005$ | 475 | $1.386 \pm 0.009$ |
| 333 | $1.466 \pm 0.007$ | 500 | $1.377 \pm 0.009$ |

calculated melting point of 360 K (see below) is $1.450 \pm 0.007$ g/cm³. The liquid-state density at the experimental melting temperature, 333 K, was calculated to be $1.466 \pm 0.007$ g/cm³. This temperature, 333 K, is below the calculated melting point of $360 \pm 10$ K, and thus, the computed density is that of a supercooled state. At the experimental melting point, the density difference of the solid and liquid is approximately 8%, which is typical of the observed differences for most materials. No experimental value for the density of liquid [patr][Br] has been reported to our knowledge.

The effect on the solid-state structure at 300 K of increasing the pressure over the range 0–7.5 GPa is shown in Figure 4, in which the Br–Br radial distribution functions (RDFs) at 0.5 GPa (solid curve), 4.0 GPa (dot–dashed curve), and 7.0 GPa (dashed curve) are plotted. Increasing the pressure has the opposite effect of increasing the temperature. By increasing the pressure, peaks in the RDF shift to smaller distances and generally become larger. This is due to the compression of the lattice and indicates increasing rotational and translational order with increasing pressure. The doublet in the first main peak is
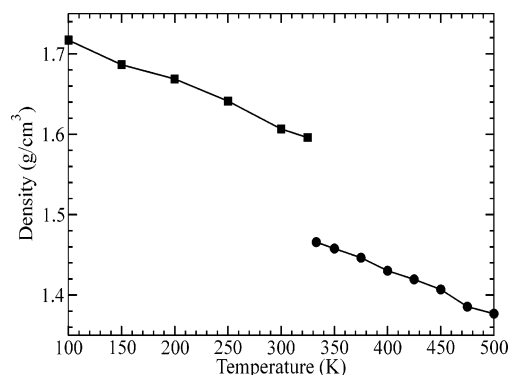
**Figure 3.** Density of [patr][Br] between 100 and 500 K from direct MD solid-state and liquid-state simulations.
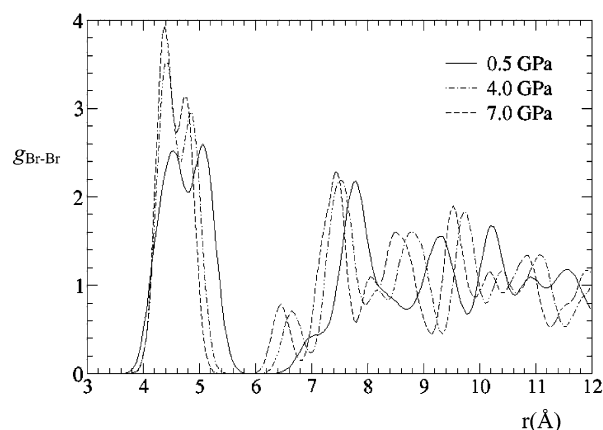
**Figure 4.** Br–Br radial distribution function for solid [patr][Br] at 300 K at three pressures. The peaks shift to smaller distances and more structural features appear at high pressures as a result of the compression of the unit cell and loss of translational freedom.
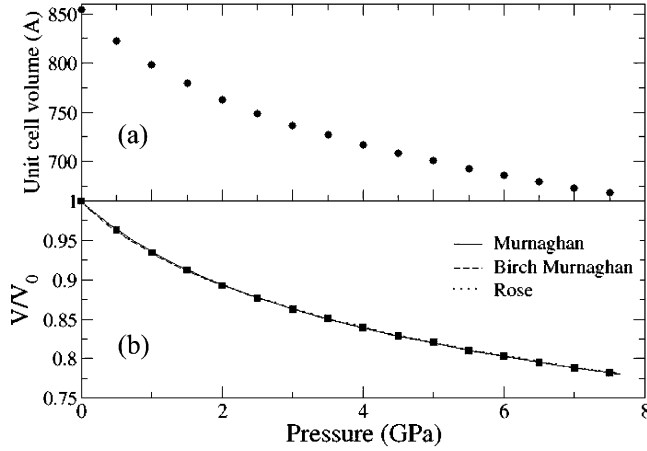
**Figure 5.** (a) Variation of the unit cell volume, $V$, of [patr][Br] with pressure at 300 K. There is a 22% reduction in the unit cell as the pressure is increased from 1 atm to 7.5 GPa. (b) The same data of part a plotted as the ratio of the volume of the unit cell to the volume at atmospheric pressure. This representation is fit to the Murnaghan equation, the Birch−Murnaghan equation, and the equation of state of Rose and co-workers.[34]

**TABLE 5: Pressure Variation of the Super Cell Volume for Solid [patr][Br] at 300 K**

| pressure (GPa) | $V$ (Å³) | pressure (GPa) | $V$ (Å³) |
|---|---|---|---|
| 0.5 | 29620.5 | 4.5 | 25501.8 |
| 1.0 | 28740.5 | 5.0 | 25237.6 |
| 1.5 | 28058.3 | 5.5 | 24933.2 |
| 2.0 | 27450.4 | 6.0 | 24693.9 |
| 2.5 | 26959.1 | 6.5 | 24462.4 |
| 3.0 | 26531.6 | 7.0 | 24227.4 |
| 3.5 | 26178.1 | 7.5 | 24047.1 |
| 4.0 | 25811.5 | | |

due to the presence of two types of nearest-neighbor bromide ions in the unit cell (see Figure 2).

The pressure dependence of the unit cell volume, $V$, and ratio of the unit cell volume at each pressure to the volume at atmospheric pressure, $V_0$, are given in Table 5 and plotted in Figure 5. The pressure dependence of the volume is fit to the Murnaghan equation[31,32] (eq 5a), the third-order Birch−Murnaghan equation[33] (eq 5b), and the equation of state of Rose et al.[34] (eq 5c)

$$P(V) = \frac{B_0}{B_0'}\left[\left(\frac{V_0}{V}\right)^{B_0'} - 1\right] \tag{5a}$$

$$P(V) = \frac{3}{2}B_0\left[\left(\frac{V}{V_0}\right)^{-7/3} - \left(\frac{V}{V_0}\right)^{-5/3}\right]$$
$$\left\{1 - \frac{3}{4}(4 - B_0')\left[\left(\frac{V}{V_0}\right)^{-2/3} - 1\right]\right\} \tag{5b}$$

$$P(V) = 3B_0\left[1 - \left(\frac{V}{V_0}\right)^{1/3}\right]\left(\frac{V}{V_0}\right)^{-2/3}$$
$$\exp\left\{\frac{3}{2}(B_0' - 1)\left[1 - \left(\frac{V}{V_0}\right)^{1/3}\right]\right\} \tag{5c}$$

where $B_0 = -V(\partial P/\partial V)_{V_0}$ is the bulk modulus at atmospheric pressure and $B_0' = \mathrm{d}B_0/\mathrm{d}P$ is the pressure derivative of the bulk modulus. The values of the parameters obtained by fitting the results in Table 5 to the equations of state are given in Table 6, and the fits are plotted along with the calculated pressure dependence of the volume in Figure 5b. The excellent fit of the solid-state compressibility data shows that the three equations can be used to model the high-pressure behavior of solid [patr]-

**TABLE 6: Solid [patr][Br] Bulk Modulus at Atmospheric Pressure, $B_0$, and the Pressure Derivative of the Bulk Modulus, $B_0'$, Calculated from the Murnaghan Equation, the Third-Order Birch−Murnaghan Equation, and the Equation of State of Rose and Co-workers[34]**

| fit parameters | Murnaghan equation | Birch−Murnaghan equation | EOS of Rose and co-workers |
|---|---|---|---|
| $B_0$ (GPa) | 11.95 | 10.62 | 11.02 |
| $B_0'$ | 6.71 | 9.58 | 8.55 |

[Br]. This information could be useful in potential applications of [patr][Br] as a high-energy material.

The RDFs for the Br−Br, $C_R$−Br, and $C_W$−Br pairs from liquid and solid [patr][Br] simulations at the experimental melting point (333 K) are shown in Figure 6. In the liquid phase, there are no long-range structural correlations, but the first peaks in the $C_R$−Br and $C_W$−Br RDFs, which represent ion-pair association, are not shifted appreciably relative to their positions in the solid.

The structures of solid and liquid [patr][Br], as shown by the RDFs of Figure 6, have aspects similar to those of the molten alkali halide salts.[35,36] The anion−cation RDFs, represented by the $C_W$−Br and $C_R$−Br RDFs have sharp first peaks at ≈3.6 Å, the position of which does not change appreciably upon melting. Upon melting, the $C_W$−Br peak shows asymmetric broadening such that the relatively sharp minima of $C_W$−Br and $C_R$−Br RDFs in the liquid state coincide at ≈4.4 Å. Melting does not cause a similar asymmetric broadening of the $C_R$−Br RDF. This difference in behavior can be due to the stronger electrostatic charge on the $C_R$ atoms ($+0.3e$) compared to the $C_W$ atoms ($+0.2e$). The relatively sharp first minima in the $C_W$−Br and $C_R$−Br RDFs indicates a moderate rate of ion exchange
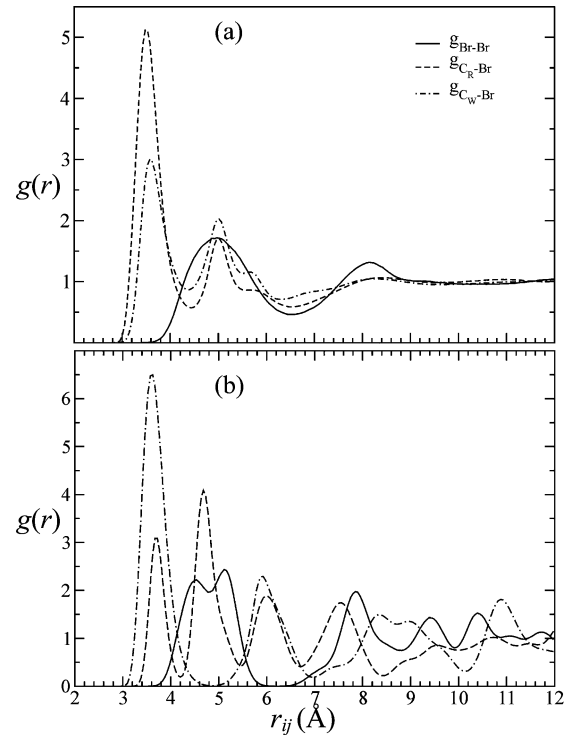


**Figure 6.** (a) Br−Br, $C_R$−Br, and $C_W$−Br radial distribution functions for liquid [patr][Br] at the experimental melting point, 333 K. (b) The Br−Br, $C_R$−Br, and $C_W$−Br radial distribution functions for solid [patr]-[Br] at the experimental melting point, 333 K. The locations of the first peak in the $C_R$−Br and $C_W$−Br curves do not change significantly upon melting (see Figure 1 for atomic labels). This demonstrates that ion-pair association remains strong in the liquid state. Long-range spatial correlations are lost upon melting.

**18132** *J. Phys. Chem. B, Vol. 109, No. 38, 2005*

Alavi and Thompson
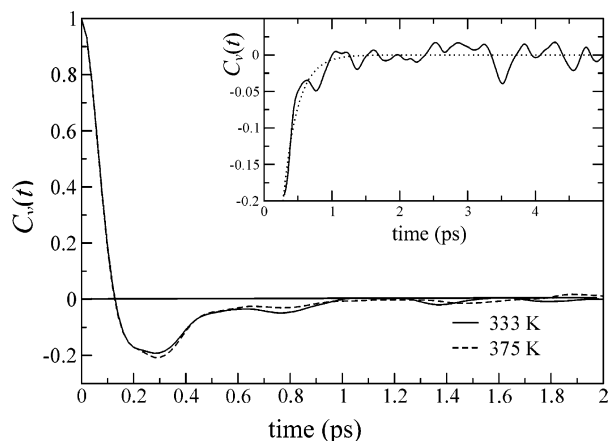


**Figure 7.** Velocity autocorrelation function, $C_v(t)$, for Br$^-$ at 333 K (solid line) and 375 K (dashed line). The negative value of the velocity autocorrelation function after $\approx 0.1$ ps shows the presence of a cage effect where each Br$^-$ is strongly coordinated by neighboring counterions. The inset shows the exponential fit of $C_v(t)$ after the minimum for the 333 K isotherm (dotted line). The time constant of the exponential fit is 0.218 ps.

between the first neighboring shell counterions and the surrounding liquid.[36]

The nonspherical nature of the cation makes the form of the cation−anion RDFs more complicated than the alkali halide analogues. The Br$^-$ can interact with the atoms of the [patr]$^+$ from directions both perpendicular and in-plane to the triazole ring. This leads to the complex structure of the liquid-state RDFs and the two sets of peaks at 3.8 and 5.0 Å in the cation−anion liquid RDFs. A similar behavior is observed for [emim][PF$_6$].[10]

The dynamic behavior of the liquid state is studied by calculating the velocity autocorrelation function (VACF), $C_v(t)$, for Br$^-$. The VACF was calculated in dimensionless form:

$$C_v(t) = \frac{\langle \mathbf{v}(0) \cdot \mathbf{v}(t) \rangle}{\langle \mathbf{v}(0) \cdot \mathbf{v}(0) \rangle} \tag{6}$$

where $\mathbf{v}(t)$ is the velocity of Br$^-$ and the broken brackets represent an ensemble average. The computed VACFs from direct liquid-state NVE simulations at 333 and 375 K are shown in Figure 7. The VACF becomes negative after $\approx 0.1$ ps. The negative VACF corresponds to a "cage effect" that extends up to $\sim 2$ ps after which the VACF for Br$^-$ oscillates about zero. The simulation results are fit by $C_v(t) = -0.67 \exp(-t/0.218)$, which is shown in the inset of Figure 7 by the dotted line. The exponential tail of the VACF of [patr][Br] is similar to the behavior observed in liquid butane[37] and nitromethane[38] and is in contrast to the power law $C_v(t) = at^{-d/2}$ long-time tail decay observed for hard-disk and hard-sphere fluids, where $a$ is a temperature-dependent constant and $d$ is the dimensionality of the system.[39]

The mean-square displacement (MSD) is defined by

$$\Delta |\mathbf{r}(t)|^2 = \frac{1}{N} \left\langle \sum_{i=1}^{N} \left| \mathbf{r}_i(t) - \mathbf{r}_i(0) \right|^2 \right\rangle \tag{7}$$

where $\mathbf{r}_i(t)$ is the location of atom $i$ at time $t$. The MSDs for liquid-state simulations for the Br$^-$ and the C$_R$ atom (see Figure 1 for atomic labels) are shown in Figure 8 for 333 and 375 K. The MSD for the C$_R$ atom is assumed to be representative of the [patr]$^+$ ion. The short-time ballistic motion of the atoms occurs for times up to $\sim 0.5$ ps. The Br$^-$ is more mobile than
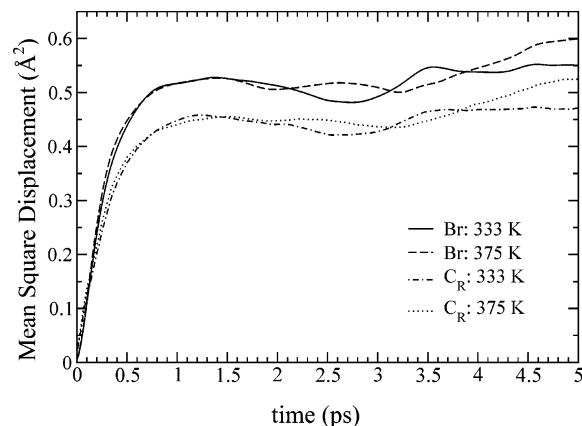


**Figure 8.** Mean-square displacement for Br$^-$ and C$_R$ (see Figure 1 for atomic labels) at 333 and 375 K. The short-time ballistic motion regime extends to about 0.5 ps. The mobility of Br$^-$ is generally greater than that of [patr]$^+$, and the mobility of both ions increases with temperature.
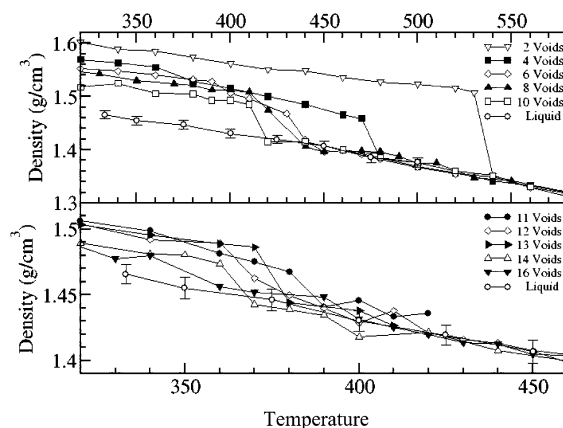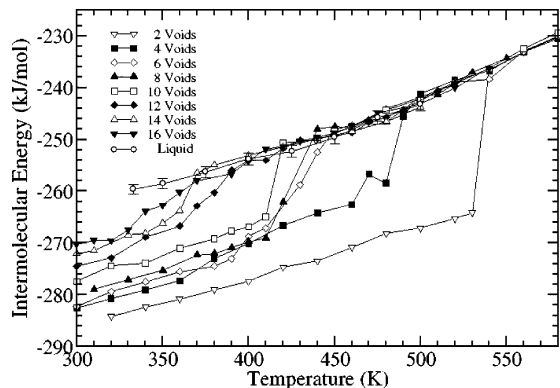


**Figure 9.** Variations of the density with temperature for simulations with 2, 4, 6, 8, 10, 11, 12, 13, 14, and 16 voids and for direct liquid-state simulations. The temperature of the onset of the density drop is taken to be the calculated melting point.

the cation, and the long-time mobilities of both ions are seen to increase at the higher temperature (375 K).

**B. Melting.** The initial configuration for the melting simulations was the experimental crystal structure at 100 K. Unlike our previously reported melting simulations of nitromethane,[6] ammonium dinitramide,[8] ammonium nitrate,[9] and 3-ethyl-1-methylimidazolium hexafluorophosphate,[10] the direct heating of a perfect crystal did not lead to melting even when the temperature was equilibrated to values as high as 600 K and simulation runs as long as 1 ns. We believe this is due to the geometrical packing of the triazolium ring and the long-chain alkyl groups on [patr]$^+$ which restrict the freedom of motion of the molecules and lead to slow equilibration.

Simulations were performed for supercells with 2, 4, 6, 8, 10, 11, 12, 13, 14, and 16 randomly located voids, with each void being one ion pair. The computed average values of the density and intermolecular energy for the final converged states at temperatures over the range 300−600 K are shown in Figures 9 and 10, respectively.

The variation of the density of [patr][Br] as a function of temperature for simulations with different void numbers is shown in Figure 9. The drop in density upon melting in a finite-time MD simulation is sharp for the simulations with two and four voids, but as more voids are introduced in the supercell, this transition occurs over a finite temperature range. The

Solid/Liquid Properties and Melting Point of [patr][Br]

*J. Phys. Chem. B, Vol. 109, No. 38, 2005* **18133**



**Figure 10.** Variations of the intermolecular energy with temperature for simulations with 2, 4, 6, 8, 10, 12, 14, and 16 voids and for direct liquid-state simulations. The temperature of the onset of the energy rise is taken to be the calculated melting point.

temperature of the onset of the density drop (or the jump in intermolecular energy) is used as the melting point.[9,10]

Prior to the onset of melting, the density of the solid state decreases smoothly as the temperature is increased. The densities of liquid [patr][Br] at temperatures between 333 and 500 K from direct liquid-state simulations are also given in Figure 9 for reference along with the errors limits for the liquid densities. These errors are characteristic of all calculated density points in Figure 9. For the simulation with two voids, the onset of the density drop at 530 K signifies the beginning of melting. The uncertainty in the calculated melting point is roughly 10 K, which is the range of uncertainty in the temperature from the MD simulations. In the two-void simulation, the solid is obviously superheated in comparison to the experimental melting point of 333 K. Simulations at different temperatures have been run for supercells with 4, 6, 8, 10, 11, 12, 13, 14, and 16 randomly introduced vacancies. The variation of density with temperature for these cases is also shown in Figure 9. As more voids are introduced into the supercell, the calculated melting point shifts to lower values. After melting, the densities calculated from simulations with different numbers of voids all converge to a common liquid-state value. This shows that all high-temperature simulations are properly converged to the true liquid state. The melting temperatures for the simulations with 12, 13, and 14 voids are well converged to a value of ≈360 K. The melting points correspond to the "plateau" region in a plot of the melting point as a function of the number of voids. A discernible drop in the density is no longer observed for simulations with 16 voids or greater in the supercell (see Figure 9). This indicates that the initial starting configuration for the 16-void simulation does not include large enough isolated solid-phase regions to give a clear melting transition and the 16-void simulation is beyond the melting point plateau.[3–10] The melting temperatures from simulations with different numbers of voids are given in Table 7.

The values of the intermolecular energy, $E_{inter} = E_{vdW} + E_{Coul}$, are also given for simulations with various numbers of voids and at various temperatures in Figure 10. The intermolecular energy from direct liquid-state simulations and the error limits of the intermolecular energies of the liquid are given for comparison. The error limits are characteristic of all energies in the simulations. There is a discontinuous rise in intermolecular energy at the onset of melting. This temperature is taken as the melting point. As with density, the jump in intermolecular energy shifts to lower temperatures as more voids are introduced into the supercell. The energies from all simulations converge to the liquid-state value at temperatures beyond the melting

**TABLE 7: Melting Point Determined from the Density, $\rho$, Intermolecular Energy, $E_{inter}$, and Lindemann Index, $\delta$, as Functions of the Numbers of Voids**

| | $T_{mp}$ (K) | | |
| number of voids | $\rho$ | $E_{inter}$ | $\delta$ |
|---|---|---|---|
| 2 | 530 | 530 | 530 |
| 4 | 470 | 480 | 480 |
| 6 | 430 | 420 | 440 |
| 8 | 410 | 410 | 430 |
| 10 | 410 | 410 | 400 |
| 11 | 380 | | |
| 12 | 360 | 360 | 370 |
| 13 | 370 | | |
| 14 | 360 | 360 | 360 |

point. In Figure 10, similar to the case of density shown in Figure 9, a converged melting temperature is obtained for simulations with 12 and 14 voids, which constitute the plateau temperature. The intermolecular energy for the simulations with 16 voids does not show a sharp melting transition. The melting points obtained from Figure 10 for different numbers of voids are summarized in Table 7.

The Lindemann index, $\delta$, is defined as

$$\delta = \frac{2}{N(N-1)} \sum_{i<j} \frac{\sqrt{\langle r_{ij}^2 \rangle_t - \langle r_{ij} \rangle_t^2}}{\langle r_{ij} \rangle_t} \qquad (8)$$

where $r_{ij}$ is the separation of any pair of particles $i$ and $j$ and $\langle...\rangle_t$ which represents a time average is also used to characterize melting. Molecules and ions in solids are confined to lattice sites, and thus, the Lindemann index is small. Upon melting, the Lindemann index can increase by as much as a factor of 3. The center-of-mass positions of both the $[patr]^+$ and $[Br]^-$ ions were included in the calculation of the Lindemann index. The summation indices $i$ and $j$ are over the center-of-mass separations of all anions and cations in the supercell. The variation of the Lindemann index with temperature is shown in Figure 11 for simulations with 2–16 voids. The temperature at which the slope of the Lindemann index begins to increase is taken as the melting point. The melting points determined by the Lindemann index (see Table 7) decrease as the number of voids in the simulation cell are increased, and the melting points obtained are in accord with those determined from the density and the intermolecular energy.
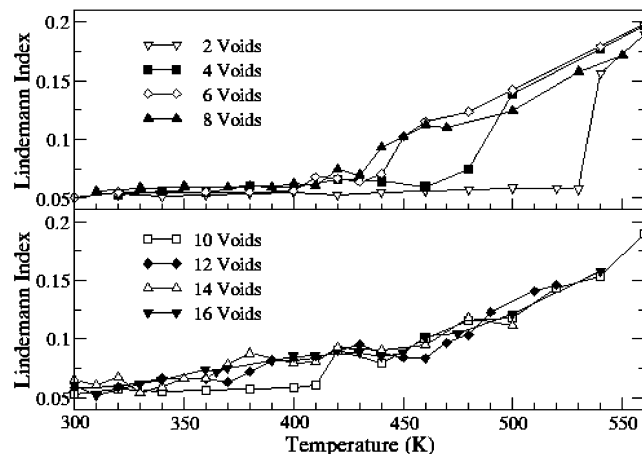


**Figure 11.** Lindemann index as a function of temperature for simulations with various numbers of voids. The melting point is taken to be the temperature at which the slope of the Lindemann index starts to rapidly increase. The melting points determined from this figure are given in the last column of Table 7.

**18134** *J. Phys. Chem. B, Vol. 109, No. 38, 2005*

Alavi and Thompson
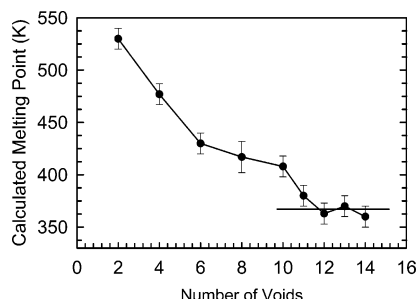


**Figure 12.** Variation of the calculated melting point for [patr][Br] as a function of the number of voids introduced in the initial configuration of the supercell. The plateau region can be observed at 360 K.

The average values of the melting point for the simulations as determined from the density, internal energy, and Lindemann index are plotted in Figure 12 as functions of the number of voids in the simulation. The calculated melting point drops as the number of voids in the simulation supercell is increased. A plateau in the melting point values is reached at $360 \pm 10$ K for 12 and 14 voids. Fourteen voids correspond to about 10% of the original number of atoms (144) in the simulation.

## 5. Summary and Conclusions

The physical properties of solid and liquid [patr][Br] have been calculated with a force field based on that of Canongia Lopes et al.,[18] modified with the GAFF and ab initio electrostatic natural population analysis charges. The calculated solid-state density is within 4% of the experimental density at 100 K. Other than the melting point and the X-ray crystal structure, the density of the solid is, to our knowledge, the only measured property for [patr][Br]. Fitting the volumetic behavior of solid [patr][Br] to the equations of state (eq 5) at high pressures yields $B_0 \approx 11$ GPa. Liquid [patr][Br] shows a strong degree of ion-pair association. The velocity autocorrelation function of Br$^-$ in the liquid quickly becomes negative and has a long-time exponential tail which is characteristic of systems with cage effects where each ion is strongly correlated to neighboring counterions. Studies of the root-mean-square displacement of Br$^-$ and the $C_R$ atom show that that the ballistic motion regime extents to about 0.5 ps. As expected, the mobility of Br$^-$ is generally greater than [patr]$^+$.

The method of void-induced melting has been used to determine the melting point of [patr][Br]. The calculated melting point from studies of the variation of the intermolecular energy, molar volume, and Lindemann was determined to be 360 K which is in reasonable agreement with the experimental melting point 333 K.

The force field is sufficient to predict the physical properties of [patr][Br] to within 10%. The results reported here add support for our observations that generally available force fields can be used to predict the melting points of complex materials to within 10% of the experimental values.[7-10] This provides a valuable tool for exploring new materials if indeed melting points can be predicted without specifically designing force fields.

## References and Notes

(1) Welton, T. *Chem. Rev.* **1999**, *99*, 2071.

(2) Rogers, R. D., Seddon, K. R., Eds. *Ionic Liquids as Green Solvents. Progress and Prospects*; ACS Symposium Series 856; American Chemical Society: Washington, DC, 2003.

(3) Lutsko, J. F.; Wolf, D.; Phillpot, S. R.; Yip, S. *Phys. Rev. B* **1989**, *40*, 2841.

(4) Solca, J.; Dyson, A. J.; Steinebrunner, G.; Kirchner, B.; Huber, H. *Chem. Phys.* **1997**, *224*, 253.

(5) Solca, J.; Dyson, A. J.; Steinebrunner, G.; Kirchner, B.; Huber, H. *J. Chem. Phys.* **1998**, *108*, 4107.

(6) Agrawal, P. M.; Rice, B. M.; Thompson, D. L. *J. Chem. Phys.* **2003**, *118*, 9680.

(7) Agrawal, P. M.; Rice, B. M.; Thompson, D. L. *J. Chem. Phys.* **2003**, *119*, 9617.

(8) Velardez, G. F.; Alavi, S.; Thompson, D. L. *J. Chem. Phys.* **2003**, *119*, 6698.

(9) Velardez, G. F.; Alavi, S.; Thompson, D. L. *J. Chem. Phys.* **2004**, *120*, 9151.

(10) Alavi, S.; Thompson, D. L. *J. Chem. Phys.* **2005**, *122*, 154704.

(11) Luo, S.-N.; Ahrens, T. J. *Appl. Phys. Lett.* **2003**, *82*, 1836.

(12) Sorescu, D. C.; Alavi, S.; Thompson D. L. Theoretical and Computational Studies of Energetic Salts. In *Chemistry at Extreme Conditions*; Manaa, M. R., Ed.; Elsevier: Amsterdam, The Netherlands, 2005.

(13) Morris, J. R.; Wang, C. Z.; Ho, K. M.; Chan, C. T. *Phys. Rev. B* **1994**, *49*, 3109. Belonoshko, A. B.; Ahuja, R.; Johansson, B. *Phys. Rev. Lett.* **2000**, *84*, 3638. Morris, J. R.; Song, X. *J. Chem. Phys.* **2002**, *116*, 9352.

(14) Frenkel, D.; Ladd, A. J. C. *J. Chem. Phys.* 1984, *81*, 3188. Frenkel, D.; Smit, B. *Understanding Molecular Simulation*; Academic Press: San Diego, CA, 2000.

(15) Grochola, G. *J. Chem. Phys.* **2004**, *120*, 2122.

(16) Eike, D. M.; Brennecke, J. F.; Maginn, E. J. *J. Chem. Phys.* **2005**, *122*, 14115.

(17) Luo, S.-N.; Strachan, A.; Swift, D. C. *J. Chem. Phys.* **2004**, *120*, 11640.

(18) Canongia Lopes, J. N.; Deschamps, J.; Pádua, A. A. H. *J. Phys. Chem. B* **2004**, *108*, 2038; **2004**, *108*, 11250 (erratum).

(19) Cornell, W. D.; Cieplak, P.; Bayly, C. L.; Gould, I. R.; Merz, K. M., Jr.; Ferguson, D. M.; Spellmeyer, D. C.; Fox, T.; Caldwell, J. W.; Kollman, P. A. *J. Am. Chem. Soc.* **1995**, *117*, 5179.

(20) Jorgensen, W. L.; Maxwell, D. S.; Tirado-Rives, J. *J. Am. Chem. Soc.* **1996**, *118*, 11225.

(21) Drake, G.; Hawkins, T.; Tollison, K.; Hall, L.; Vij, A.; Sabowski, S. In *Ionic Liquids III: Fundamentals, Progress, Challenges, and Opportunities*; Rogers, R. D., Seddon, K. R., Eds.; ACS Symposium Series 901−902; American Chemical Society: Washington, DC, 2005.

(22) (a) Glendening, E. D.; Reed, A. E.; Carpenter, J. E.; Weinhold, F. *NBO*, version 3.1, implemented in ref 23. (b) Foster, J. P.; Weinhold, F. *J. Am. Chem. Soc.* **1980**, *102*, 7211. (c) Reed, A. E.; Curtiss, L. A.; Weinhold, F. *Chem. Rev.* **1988**, *88*, 899.

(23) Frisch, M. J.; et al. *Gaussian 98*, revision A.7; Gaussian, Inc.: Pittsburgh, PA, 2001.

(24) Forester, T. R.; Smith, W. *DL_POLY 2.10*; CCLRC: Daresbury Laboratory, 1995.

(25) Nosé, S. *J. Chem. Phys.* **1984**, *81*, 511.

(26) Hoover, W. G. *Phys. Rev. A* **1985**, *31*, 1695.

(27) Melchionna, S.; Ciccotti, G.; Holian, B. L. *Mol. Phys.* **1993**, *78*, 533.

(28) Allen, M. P.; Tildesley, D. J. *Computer Simulation of Liquids*; Oxford Science Publications: Oxford, U.K., 1987.

(29) Gibson, K. D.; Scheraga, H. A. *J. Phys. Chem.* **1995**, *99*, 3752.

(30) Kittel, C. *Introduction to Solid State Physics*, 7th ed.; Wiley: New York, 1996.

(31) Murnaghan, F. D. *Finite Deformation of an Elastic Solid*; Dover: New York, 1951; p 73.

(32) Anderson, D. L. *Theory of the Earth*; Blackwell Scientific Publications: Boston, MA, 1989.

(33) Birch, F. *Phys. Rev.* **1947**, *71*, 809.

(34) Rose, J. H.; Smith, J. R.; Guinea, F.; Ferrante, J. *Phys. Rev. B* **1984**, *29*, 2963.

(35) Blander, M., Ed.; *Molten Salt Chemistry*; Interscience: New York, 1964.

(36) Tosi, M. P.; Price, D. L.; Saboungi, M.-L. *Ann. Rev. Phys. Chem.* **1993**, *44*, 173.

(37) Daivis, P. J.; Evans, D. J. *J. Chem. Phys.* **1995**, *103*, 4261.

(38) Sorescu, D. C.; Rice, B. M.; Thompson, D. L. *J. Phys. Chem. A* **2001**, *105*, 9336.

(39) Haile, J. M. *Molecular Dynamics Simulation: Elementary Methods*; Wiley: New York, 1992.